Hindawi
Journal of Nanotechnology
Volume 2019, Article ID 6802125, 9 pages
https://doi.org/10.1155/2019/6802125

Research Article

Ablation of Hepatic Tumors through the Use of a Novel Magnetic Nanocomposite Probe: Magnetic Characterization and Finite Element Method Analysis

Yvonne Konku,[1] John Kutor,[1] Abu Yaya,[2] and Kwabena Kan-Dapaah[1]

[1]*Department of Biomedical Engineering, University of Ghana, P. O. Box LG 25, Legon, Ghana*
[2]*Department of Materials Science and Engineering, University of Ghana, P. O. Box LG 25, Legon, Ghana*

Correspondence should be addressed to Kwabena Kan-Dapaah; kkan-dapaah@ug.edu.gh

Received 8 July 2018; Revised 25 December 2018; Accepted 10 January 2019; Published 3 March 2019

Academic Editor: Paresh Chandra Ray

The authors recently proposed a novel system for thermoablation—based on nanoheating—that can potentially overcome limitations associated with previously reported techniques. The aim of this study was to evaluate the therapeutic performance of the system in the ablation of hepatic tissue, the most frequently ablated. A model nanocomposite system, maghemite nanoparticle-filled polydimethylsiloxane, was prepared, and its magnetic properties were studied as a function of nanoparticle concentration. On the basis of measured magnetic properties, a 3D finite element method (FEM) model was used to explore the development of temperature and thermal damage in nonperfused and fully perfused tissue using alternating magnetic field (AMF) parameters that are acceptable for human use. The FEM model was tested for its validity using an analytical model. The saturation magnetization increased to about 9% of the value of pure maghemite nanoparticles over the range of volume fraction (vol. %) between 1 and 5%. Lesion sizes were shown to be greatly affected by tissue perfusion and time. FEM predictions showed good agreement with results obtained with an analytical model to within 7%. Probes fabricated with magnetic nanocomposite can potentially be used to achieve reasonable lesion sizes in hepatic tissues using human-safe AMF parameters.

1. Introduction

Hepatocellular carcinomas (HCC), which is the most common type of liver cancer, originate from hepatocytes, the main liver cells. It is the third major cause of cancer death worldwide with the highest incidence rates in less developed countries [1]. The main curative treatment options include resection, transplantation, or ablation. Resection is limited to patients with small localized tumors and well-preserved liver function [2]. Unavailability of donors limits the applicability of transplantation [2]. Minimally invasive locoregional ablation is the most frequently used treatment, due to their potential to localize treatment and reduce injuries to surrounding healthy tissue. Therefore, there is a need for minimally invasive nonsurgical techniques that can overcome challenges associated with conventional methods to enhance treatment.

Common locoregional therapies include percutanous ethanol injection, cryoablation, laser ablation, microwave ablation, high-focused ultrasound, and radiofrequency ablation (RFA). RFA is the most widely used technique due to its general availability and recent technical advances; however, issues such as the need for high-current radiofrequency to increase lesion sizes lead to an increased risk of skin burns that in turn limits lesion sizes [3–5]. The incidence of skin burns after RFA ranges from 0.1–3.2% for second-/third-degree skin burns and up to 33% for first-degree burns [6].

The unique heat generating capabilities of nanomaterials have been exploited to develop smart and efficient systems for cancer therapy. Promising inorganic nanomaterials—metallic [7] and magnetic [8]—have been demonstrated to enable localized and/or multimodal treatment that can potentially enhance treatment efficacy.

[9] The introduction of these nanomaterials into polymer matrix to form nanocomposites offers opportunities for the development of novel biomedical devices for cancer treatment [10, 11]. The authors have recently reported a novel nanocomposite probe for thermoablation of cancer cells [12, 13]. The probe is essentially a cannula with a distal heat generating magnetic nanocomposite tip and a proximal insulated shaft. *In vivo* predictions demonstrated the feasibility of the probe to achieve hyperthermic or ablative levels in postoperative breast tissue.

In this paper, we present an evaluation of the therapeutic performance of our novel probe during the ablation of hepatic tumor, which has been demonstrated to be the most frequently ablated [2]. First, we prepared samples of a model nanocomposite, maghemite ($\gamma - Fe_2O_3$) nanoparticle (MNP) filled polydimethylsiloxane (PDMS), containing varying concentrations of nanoparticles and measured their saturation magnetization. A 3D finite element method (FEM) model was used to perform a parametric study to investigate the development of temperature and thermal damage in nonperfused and fully perfused tissue using alternating magnetic field (AMF) parameters that are acceptable for human use. The FEM model was tested for its validity using an analytical model. The implications of the results are then discussed for the application of the probe for cancer treatment.

2. Materials and Methods

2.1. Materials. The materials that were used in this study included maghemite ($\gamma - Fe_2O_3$) nanoparticles (high purity, 99.5%, 20 nm, US Research Nanomaterials Inc., Houston, TX, USA) and PDMS (Sylgard 184 silicone elastomer kit, Dow Corning Corp., Auburn, MI, USA). These materials were used as received.

2.2. Sample Preparation. Three types of nanocomposites, designated as MNP-1, MNP-2, and MNP-5—with volume fractions, ϕ, of 1, 2, and 5 vol. % of MNP respectively—were prepared. The sample were prepared by, first, adding the nanoparticles to the PDMS elastomer base and stirring the mixtures thoroughly with a spatula for 15 mins to ensure uniform nanoparticle distribution and also minimize clustering. Then, the curing agent of the PDMS base was added at a weight ratio of 10 : 1 and, again, stirred with the spatula to produce a uniform mixture with adequate cross-linking. To ensure that air bubbles were completely removed, the resulting mixtures were placed in a glass beaker connected to a vacuum pump for about 30 minutes. The resulting MNP-PDMS nanocomposite mixtures were poured into molds and baked in an oven at 100°C for 43 minutes.

2.3. Magnetic Characterization. Magnetic measurements were carried out using the superconducting quantum interface device (SQUID) magnetometer, MPMS XL-5 (Quantum Design, San Diego CA, USA). The magnetization curves were obtained by varying magnetic fields between 0 $MA{\cdot}m^{-1}$ and 0.4 $MA{\cdot}m^{-1}$ at a temperature of 298 K. MNPs were mounted in capsules, whereas solid nanocomposites were mounted in drinking straws. Due to the varying masses of the samples, specific magnetization values were used for our analysis.

2.4. Theory of Magnetic Heating. When a constrained MNP is exposed to an AMF, the specific losses, A ($J{\cdot}g^{-1}$), during one cycle of the AMF are defined as the area of the hysteresis loop. According to Carrey et al. [14], an experimentally measured hysteresis loop area, A, can be represented by

$$A = 4\alpha\sigma_s\mu_0 H, \tag{1}$$

where α is a dimensionless parameter that depends on the orientation of MNP's easy axes with respect to the AMF. An α value of 0.30, previously reported in [12], was used in all our analysis. σ_s ($A{\cdot}m^2{\cdot}kg^{-1}$) is the saturation magnetization, μ_0 ($H{\cdot}m^{-1}$) is the permeability of free space. H ($A{\cdot}m^{-1}$) is the amplitude of the AMF.

The heat dissipation, P ($W{\cdot}m^{-3}$), is determined by the following equation:

$$P = Af\rho_n, \tag{2}$$

where ρ_n is density of nanocomposite.

2.5. In Vivo Predictions. Finite element method (FEM) model, implemented with Comsol Multiphysics 4.3a software package (Comsol, Burlington MA, USA), was used to characterize the *in vivo* performance.

2.5.1. FEM Modeling. Figure 1(a) shows a schematic diagram of the probe used in our study. The probe is a 6 cm cannula with a distal 2 cm active nanocomposite (MNP-PDMS nanocomposite) tip and a proximal 4 cm insulated shaft (PDMS only). Its concept and mode of operation has been previously reported. [12].

The geometric model that was used in our study is shown in Figure 1. Hepatic tissue is modeled as a cylindrical block with a diameter and height of 6 cm and 12 cm, respectively. The probe is placed within the cylindrical block such that the active tip is situated at the center of cylindrical block.

The temperature distribution within the tissue is determined by the Pennes bioheat equation [15]:

$$\rho c_p \frac{\partial T}{\partial t} = \lambda\nabla^2 T + \rho_b c_b \alpha_b \omega_b \left(T_b - T\right) + Q_m + Q, \tag{3}$$

where ρ ($kg{\cdot}m^{-3}$) is the density, c_p ($J{\cdot}kg^{-1}{\cdot}K^{-1}$) is the specific heat capacity at constant pressure, λ ($W{\cdot}m^{-1}{\cdot}K^{-1}$) is the thermal conductivity. ρ_b, ω_b (s^{-1}), c_b, and T_b are the density, tissue perfusion rate, specific heat capacity, and temperature of blood, respectively. α_b is tissue state coefficient. Q_m ($W{\cdot}m^{-3}$), the metabolic heat, was ignored. Q is the heat generation term, which is defined differently for each domain. For the tissue and the insulated shaft domains, it was set to zero. For the active tip (nanocomposite), it was calculated as volumetric power as defined by equation (2)

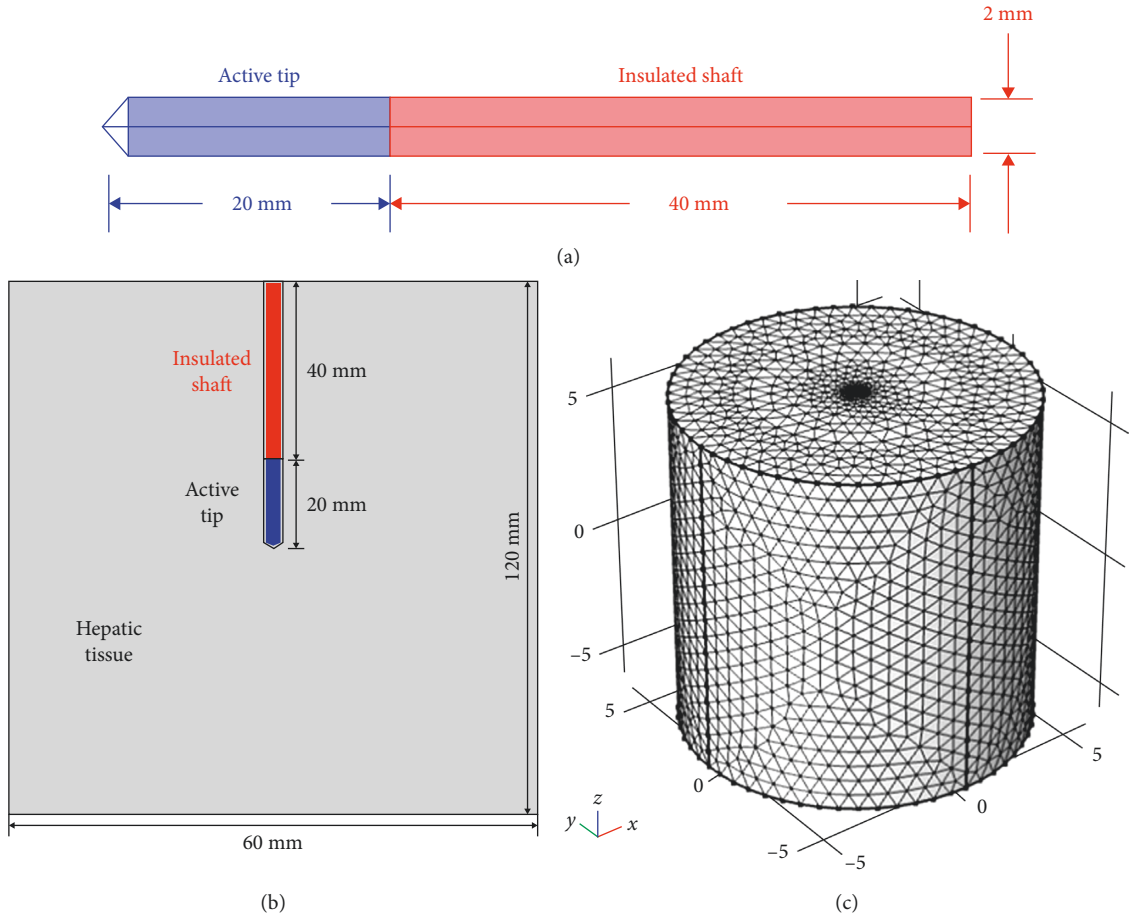

FIGURE 1: (a) Schematic of magnetic heating probe. The probe is a cannula with two main parts: a distal active tip made of a nanocomposite (blue) and a proximal insulated shaft (pink). Therapeutic treatment is achieved when the active tip is brought in contact with the target area and exposed to alternating magnetic field. (b) Schematic of the geometry model (cylindrical block: diameter, 6 cm; height, 12 cm), showing the cross section of the probe inserted in the tissue. (c) The 3D meshed model of the cylindrical block.

The boundary conditions for equation (3) were a prescribed temperature, $T = 37^{\circ}\text{C}$, on all outer surfaces; and continuity, $n \cdot (\lambda_1 \nabla \cdot T_1 - \lambda_2 \nabla \cdot T_2) = 0$, on all of interior boundaries. A temperature of 37°C (for the normal body) was used as the initial temperatures in all domains of the model.

To predict thermal damage of the tissue, the well-established Arrhenius equation was used. It is a first-order thermal-chemical rate equation that enables the determination of damage with temperature history. The damage, which is considered to be due to the transformation of native molecules through an activated state leading to cell death, is quantified using a dimensionless single parameter, Ω, as

$$\Omega(t) = S_f \int_0^t \exp\left(\frac{-E_a}{\mathrm{RT}(t)}\right) dt, \tag{4}$$

where E_a ($\text{J}\cdot\text{mol}^{-1}$) is the activation energy for the injury process, S_f (s^{-1}) is a scaling factor, and R ($\text{J}\cdot\text{mol}^{-1}\cdot\text{K}^{-1}$) is the gas constant. The values of E_a and A were obtained from [16] as 257.7 $\text{kJ}\cdot\text{mol}^{-1}$ and 7.39×10^{39} s^{-1}, respectively. In this study, $\Omega = 1$, which corresponds to a 63% percent probability of cell death, is chosen to indicate that sufficient irreversible damage has been achieved. [17] At this point, it has been reported previously that tissue perfusion ceases [18]. This corresponds to a α_b of zero. Therefore, intermediate values of α_b were calculated as 1/exp (Ω) [18].

The thermal properties of different domains used in the simulation are summarized in Table 1. The effective thermal and physical properties of the nanocomposites were estimated using the rule of mixtures. The details of the implementation are summarized in Appendix.

2.5.2. Parametric Investigations. Generally, 0.05 – 1.2 MHz and 0 – 15 $\text{kA}\cdot\text{m}^{-1}$ are considered the usable ranges for f and H of the AMF for thermotherapy. [23] However, taking patient safety and health into consideration, it is essential to ensure that the factor, Hf, does not exceed the limit that has been experimentally estimated to be 5×10^9 $A\cdot\text{m}^{-1}\cdot\text{s}^{-1}$ [24]. According to [23], the maximum human-safe field amplitude is 15 $\text{kA}\,\text{m}^{-1}$. Ablations were simulated at AMF parameters: $H = 5 - 15$ $\text{kA}\cdot\text{m}^{-1}$, step size: 5 $\text{kA}\cdot\text{m}^{-1}$, $f = 150 - 450$ kHz, and step size of 150 kHz. These ranges were selected to maintain the Hf factor below the limit. Furthermore, thermal damage was studied as a function of

Table 1: Thermal properties of the materials used in the FEM models.

Material	ρ (kg m^{-3})	c_p (J (kg K)$^{-1}$)	λ (W (m K)$^{-1}$)	ω (s^{-1})
Liver [19]	1,060	3,600	0.502	—
Blood [20]	1,000	4,180	0.543	0.0064
PDMS [21]	1,190	1,460	0.190	—
$\gamma - Fe_2O_3$ [22]	4,600	746	9.700	—

tissue perfusion and time to determinate the maximum variation in lesion size during a typical ablation where this parameter can be varied [25]. Simulations were made at ω_b–0%, 50%, and 100% of normal tissue perfusion of 0.0064 s^{-1} and t = 180 s and 300–900 s (step size: 300).

2.5.3. FEM Model Validation. The FEM model was tested for its validity using an analytical model developed by Andrä et al. [26]. The model, which predicts temperature rise due to a spherical nanocomposite, is given by

$$\Delta T_1(r,t) = \frac{PR^2}{3\lambda_2}\left[1 + \frac{q_\lambda}{2}\left(1 - \frac{r^2}{R^2}\right) + \frac{6}{\pi}q_\lambda^{3/2}q^{1/2}\frac{R}{r}\int_0^\infty f g_1\, dz\right], \quad 0 \le r \le R, \tag{5a}$$

$$\Delta T_2(r,t) = \frac{PR^3}{3\lambda_2 r}\left[1 + \frac{6}{\pi}q_\lambda\int_0^\infty f g_2 \frac{dz}{z}\right], \quad r > R, \tag{5b}$$

where P is volumetric power (equation (2)), ρ_1 is density, c_1 is heat capacity, and λ_1 is thermal conductivity of the nanocomposite, all approximated by the rule of mixtures. ρ_2, c_2, and λ_2 are the properties of liver tissue. Parameters f, g_1, g_2, q, and q_λ are abbreviations:

$$q_\lambda = \frac{\lambda_2}{\lambda_1},$$

$$q_\lambda = \frac{\rho_2 c_2}{\rho_1 c_1},$$

$$s(z) = (q_\lambda - 1)\sin z + z\cos z,$$

$$f(z,r,t) = z^{-2}\exp\left(-\frac{\lambda_1 t z^2}{\rho_1 c_1 R^2}\right) \times \frac{z\cos z - \sin z}{[s(z)]^2 + q_\lambda q(\sin z)^2},$$

$$g_1(z,r) = \sin\left(\frac{rz}{R}\right),$$

$$g_2(z,r) = s(z)\sin[k(z;r)] + (q_\lambda q)^{1/2} z \sin z \cos[k(z,r)],$$

$$k(z,r) = (q_\lambda q)^{1/2} z\left(\frac{r}{R} - 1\right). \tag{6}$$

The nanocomposite was assumed to contain 5 vol. % of MNP and PDMS; its properties were calculated using simple rule of mixtures. The radius of the sphere was taken as R = 1.5 mm. A volumetric heating power, P, of 33.7 (MW·m^{-3}), was used. The surrounding area was assumed to be liver tissue, thus the corresponding properties in Table 1 were used.

3. Results and Discussion

3.1. Materials Characterization. Figure 2 shows the magnetization curves of the MNPs and nanocomposites in magnetic fields of 45 kOe. MNPs had a saturation magnetization value, M_s, of 69.33 emu·g^{-1}. The M_s values for samples MNP-1, MNP-2, and MNP-5 were 2.37 emu·g^{-1}, 3.41 emu·g^{-1}, and 6.46 emu·g^{-1}, respectively. These values were about 3.4%, 4.9%, and 9.3%, respectively, of the M_s value obtained for pure MNP. Although M_s values of the nanocomposites increased with increasing concentration of nanoparticles, it is important to note that, at higher concentrations (about above 10% volume fraction), particle agglomeration due to factors such magnetic attraction or van der Waals forces can affect the magnetic properties and, consequently, the specific loss power [27].

3.2. In Vivo Predictions. On the basis of the magnetic measurements, we assessed the performance of the device during the heating of hepatic tissue using a parametric study.

A cross-sectional (x-z plane) view of the temperature distribution within the fully perfused tissue (Figure 3(a)) after heating for 15 mins reveals that the temperature is nonuniformly distributed with a maximum temperature, T_{at}, occurring at the center of the active tip. It can be observed that the generated heat spreads out to the surrounding tissue; therefore, the maximum tissue temperature, T_t, which occurs on the surface of the active tip, is lower. This is consistent with conduction, the main mode of heat transfer in action. Table 2 shows predictions of T_{at} and T_t for a range of AMF amplitudes (5–15.0 kA·m^{-1}) and frequencies (150–450 kHz) after 15 mins of heating for all three samples. It can be observed that the temperature difference ($T_{at} - T_t$) increases with increasing Hf factor and ϕ. For instance, for the nanocomposite containing 2 vol. %, $T_{at} - T_t$ increases from ≈ 9.7°C for the Hf factor of 1.5×10^9 A·m^{-1}·s^{-1} (H = 10 kA·m^{-1}, f = 150 kHz) to ≈ 11.8°C for the Hf factor of 4.5×10^9 A·m^{-1}·s^{-1} (H = 10 kA·m^{-1}, f = 450 kHz). Similarly, for a given Hf factor of 1.5×10^{-9} A·m^{-1}·s^{-1} (H = 10 kA·m^{-1}, f = 150 kHz), $T_{at} - T_t$ increases from ≈ 9.7°C (ϕ = 2%) to ≈ 17.6°C (ϕ = 5%). Furthermore, different H and f pairs such as H = 10 kA·m^{-1}, f = 450 kHz and H = 15 kA·m^{-1}, f = 300 kHz can be used to achieve the same temperature levels (T_{at} = 175.5°C, T_t = 116.4) for a given MNP concentration. Taking patient safety and health into consideration, it is prudent to use lower AMF values. Table 3 summarizes the heating power density (W·m^{-3}) and total heating power (W) values of the active tip of the probe that were used to obtain the temperature values in Table 2.

For our thermal damage analysis, values in the middle range of both H and f (i.e., 10 kA·m^{-1} and f = 300 kHz

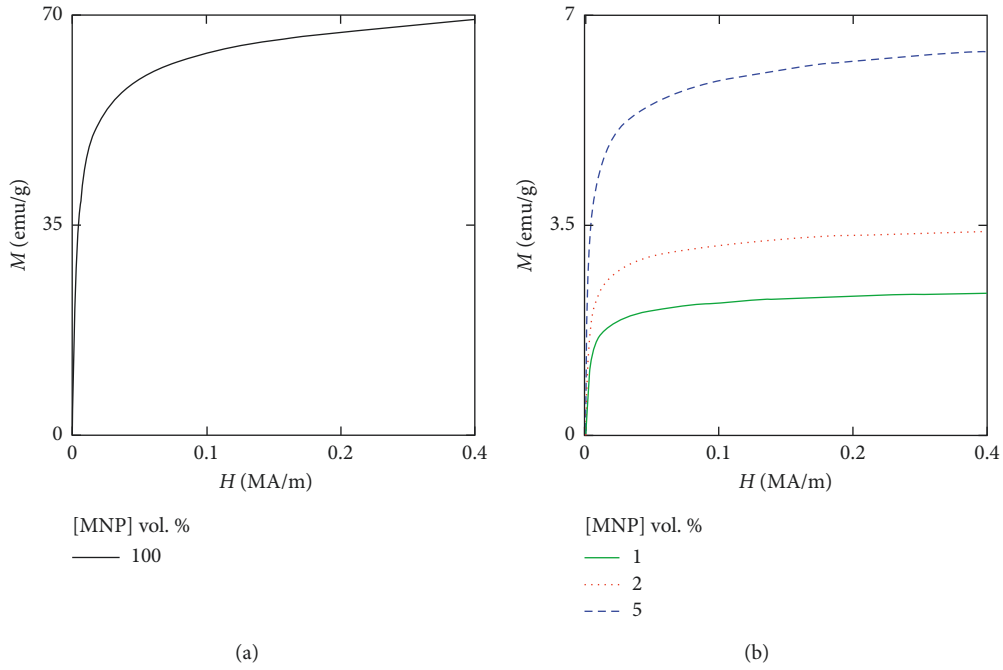

FIGURE 2: Magnetization curves of (a) maghemite ($\gamma - Fe_2O_3$) nanoparticles and (b) samples MNP-1, MNP-2, and MNP-5 under magnetic fields of 0.4 MA·m^{-1}.

respectively), resulting in $T_t = 90^\circ$C, were used. A cross-sectional (x-z plane) view of the lesion, region where tissue damage occurs, reveals its ellipsoidal shape (Figure 3(b)), which is distributed symmetrically about the active tip of the probe. Figure 3(d) shows a plot of tissue temperature and thermal damage calculated at a point 0.3 cm away from the center of the active-tip after 15 mins of heating at different rates of tissue perfusion. It can be observed that 100% thermal damage is reached a few minutes after the AMF is applied. For the case of fully perfused tissue ($\omega_b = 6.4 \times 10^{-3}$ s^{-1}), it occurs after 3 mins. The time decreases to 2 mins for the case of nonperfusion ($\omega_b = 0.0 \times 10^{-3}$ s^{-1}). This relatively fast attainment of thermal damage can be attributed to the initial heating rates, resulting in exposure of the tissue to ablative temperatures almost the entire duration of treatment. Although at distances farther away from the active tip overall temperature levels decrease, adequate thermal damage is possible due to long durations of exposure at those temperatures (Figure 3(e)). Figure 3(f) shows a plot of tissue temperature and thermal damage as function of radial distance after 15 minutes for varying rates of tissue perfusion. The data show that moving away from the active-tip thermal damage decreases more rapidly than temperature.

Table 4 summarizes lesion size development as a function of time for nonperfused ($\omega_b = 0.0 \times 10^{-3}$ s^{-1}) and fully perfused ($\omega_b = 6.4 \times 10^{-3}$ s^{-1}). The parameters used to calculate the sizes are shown in Figure 3(c). The results reveal that tissue perfusion greatly affects the development of the lesion. For instance, lesion volume increases from 1.29 cm^3 (after 3 minutes) to 11.82 cm^3 (after 15 minutes) in a nonperfused ($\omega_b = 0.0 \times 10^{-3}$ s^{-1}) tissue, representing an increase of 916%. This reduced to 293% for fully perfused is considered. At 15 mins, predicted lesion width and depth were in the range of 1.40 – 2.58 cm and 2.58 – 3.39 cm, respectively.

3.3. Model Validation. In an effort to validate the computational model, the numerical results were compared with results obtained with the analytical model developed by Andrä and co-workers [26]. Figure 4 shows the comparison of the temperature as a function of (a) time at a point ≈ 2 mm from the center of the nanocomposite (a) and distance from the center of composite (b) after 15 mins of heating. The results reveal that FEM results diverged between ≈0.5 – 7% from the analytical results. The deviations can be attributed to factors such as mesh sizing and shape of the geometry.

4. Conclusion

In this work, a combination of experiments and models was used to investigate the thermoablation of hepatic tumors through the use of a magnetic nanocomposite probe.

A model, polymer-based nanocomposites consisting of PDMS and $\gamma - Fe_2O_3$ nanoparticles, was successfully fabricated. Magnetic measurements obtained with a SQUID magnetometer showed that their saturation magnetizations, M_s, increased with increasing nanoparticle concentration to about 9% of the M_s value of pure $\gamma - Fe_2O_3$ nanoparticles over the range of volume percentages between 1 and 5%. On the basis of the magnetic measurement, the *in vivo* performance of the probe, using human-safe AMF parameters, was investigated. The results showed that reasonable lesion sizes, which are greatly affected by time and tissue perfusion, are achievable. Lesion volumes increased by 916% and 293%,

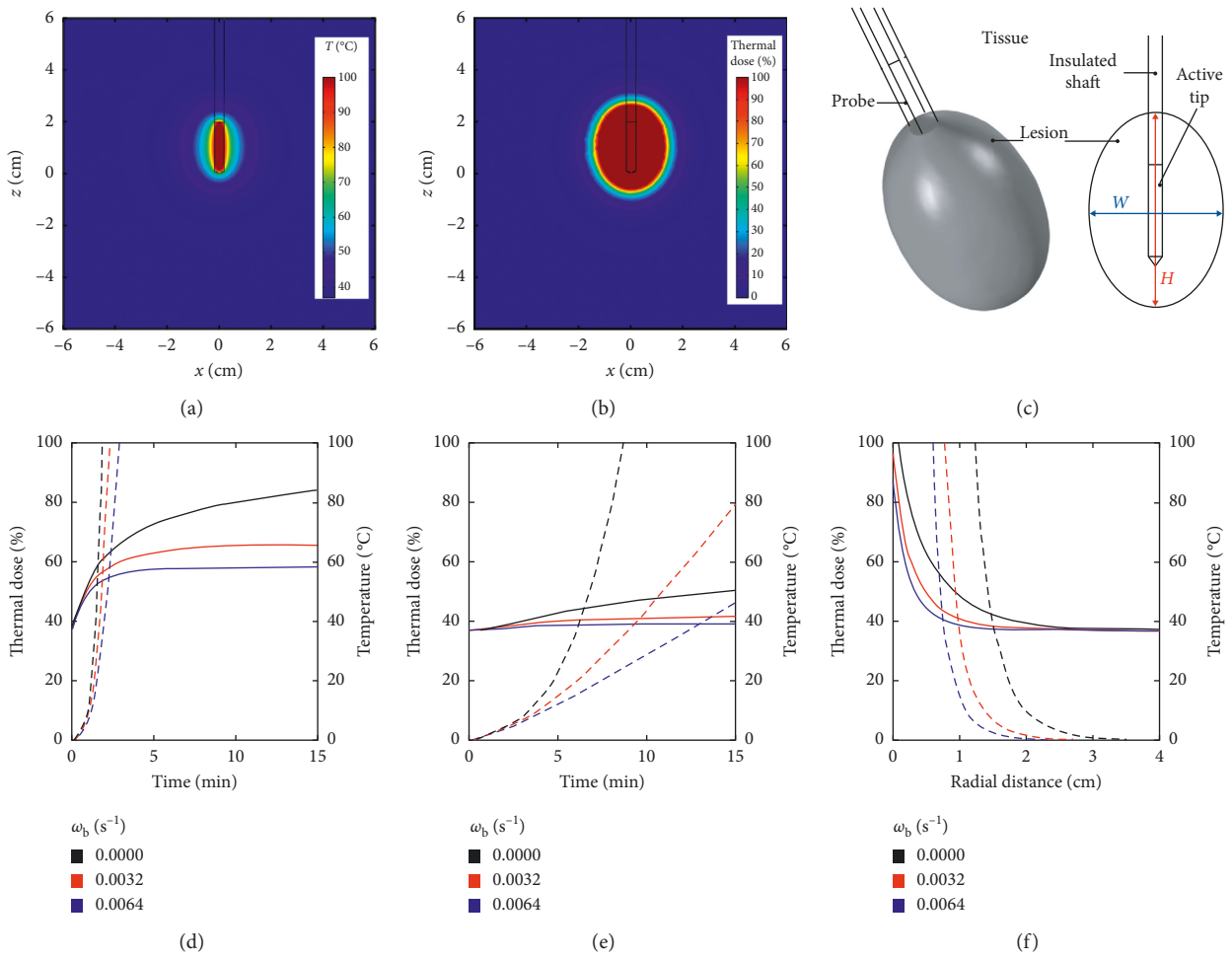

Figure 3: Cross-sectional (x-z plane) (a) temperature distribution and (b) thermal damage on the central slice. (c) A schematic of the lesion and the measured parameters. Tissue temperature (solid lines) and thermal damage (broken lines) at a distance of (d) 0.3 cm and (e) 1 cm from the outer surface of the active tip as a function of time. (f) Tissue temperature (solid lines) and thermal damage (broken lines) measured from the surface of the active tip. Study settings: t = 15 mins, ϕ = 5%, H = 10 kA·m^{-1}, and f = 300 kHz.

Table 2: Temperature predictions for a range of AMF amplitudes (5–15 kA·m^{-1}) and frequencies (150–450 kHz).

Domain	ϕ (vol. %)	σ_s (emu·g^{-1})	H = 5 kA·m^{-1} f (kHz)			H = 10 kA·m^{-1} f (kHz)			H = 15 kA·m^{-1} f (kHz)		
			150	300	450	150	300	450	150	300	450
Active tip	1	2.37	44.5	52.1	59.6	52.1	67.2	82.3	59.6	82.3	104.9
	2	3.41	48.2	59.5	70.8	59.5	82.0	104.6	70.8	104.6	138.4
	5	6.46	60.1	83.1	106.2	83.1	129.3	175.4	106.2	175.4	244.6
Tissue	1	2.37	41.3	45.5	59.6	45.5	54.0	62.5	49.8	62.5	75.3
	2	3.41	43.4	49.8	56.2	49.8	62.6	75.3	56.2	75.3	94.5
	5	6.46	50.2	63.5	76.7	63.5	90.0	116.4	76.7	116.4	156.2

for nonperfused and fully perfused tissue, respectively, between 3 and 15 mins of heating. A comparison of lesion volumes for nonperfused and fully perfused tissue at specific times show that the difference increased with time. For instance, at 3 mins, the predicted volume for a nonperfused tissue was about 2 times bigger than volume obtained for fully perfused tissue. At 15 mins, it doubled. These sizes are similar to those obtained by other probe-based thermoablation techniques reported in the literature [18, 28, 29].

The results demonstrate the potential of our magnetic nanocomposite probes to treat small ($\leq 1-3$ cm) solid hepatic tumors. Furthermore, a potential advantage of our probe over other probe-based techniques is the possibility of incorporating multimodal (heat and drugs) features.

Table 3: Power density, P (W m^{-3}), and total power, P_T (W), values of the active tip of the probe that was used to obtain the temperature predictions in Table 2.

ϕ (vol. %)	σ_s (emu·g^{-1})	H = 5 kA·m^{-1} f (kHz)			H = 10 kA·m^{-1} f (kHz)			H = 15 kA·m^{-1} f (kHz)		
		150	300	450	150	300	450	150	300	450
		Power density, P_T (MW m^{-3})								
1	2.37	2.8	5.6	8.5	5.6	11.3	17.0	8.5	17.0	25.4
2	3.41	4.4	8.9	13.3	8.9	17.8	26.7	13.3	26.7	40.0
5	6.46	11.7	23.4	35.1	23.4	46.8	70.2	35.1	70.2	105.3
		Total Power, P (W)								
1	2.37	0.2	0.3	0.5	0.3	0.7	1.0	0.5	1.0	1.5
2	3.41	0.3	0.5	0.8	0.5	1.1	1.6	0.8	1.6	2.4
5	6.46	0.7	1.4	2.1	1.4	2.8	4.3	2.1	4.3	6.4

Table 4: Comparison of lesion parameters for nonperfused ($\omega = 0.0 \times 10^{-3}$ s^{-1}) and fully perfused ($\omega = 0.0 \times 10^{-3}$ s^{-1}) tissue at different times.

Time (s)	$\omega = 0.0 \times 10^{-3}$ s^{-1}			$\omega = 6.4 \times 10^{-3}$ s^{-1}		
	Width (cm)	Depth (cm)	V (cm^{-3})	Width (cm)	Depth (cm)	V (cm^{-3})
180	1.04	2.28	1.29	0.80	2.19	0.73
300	1.42	2.50	2.64	0.98	2.30	1.16
600	2.04	2.96	6.45	1.26	2.46	2.04
900	2.58	3.39	11.82	1.40	2.58	2.65

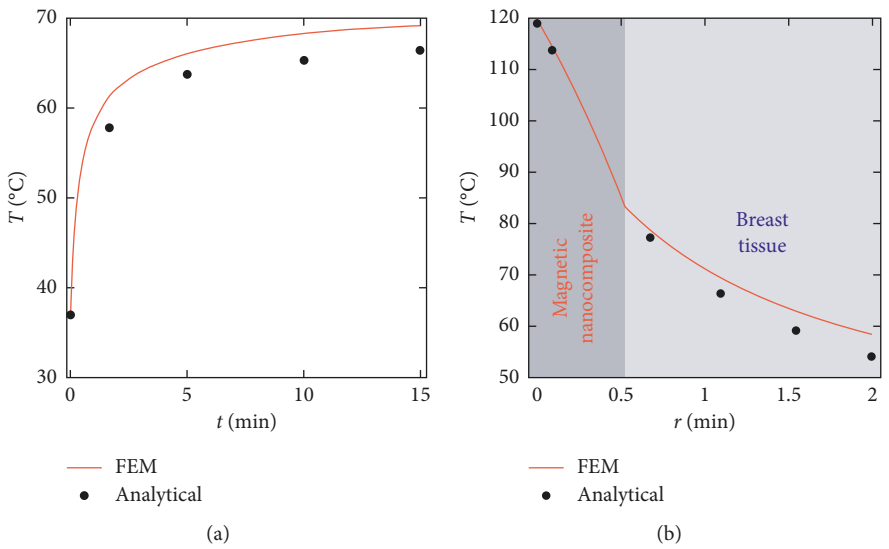

Figure 4: Comparison of temperature as function of (a) time at a point ≈ 2 mm mm from the center of the nanocomposite and (b) the distance from the center of composite after 15 mins of heating between FEM model and the analytical model by Andrä et al. [26].

Further studies, including *in vitro* and *in vivo* experiments, are needed for a realistic assessment of the probe.

Appendix

Implementation of FEM Model

The numerical analyses were performed with the FEM model COMSOL Multiphysics 4.3a software package (Comsol, Burlington MA, USA). All physical, magnetic, and thermal properties were added explicitly to the FEM model as a global definition or variable under the model node. A 3D geometric model was used for the analysis.

The temperature distribution was achieved with the bioheat heat transfer application mode. 37°C was taken as the initial temperature of the model, and all boundary conditions were specified as those outlined in Section 2 E1. The heat source was added to the bioheat transfer application mode as a user-defined heat source.

The geometric model was meshed with varying sizes of 3D triangular mesh elements. The mesh size for all calculations was defined as a physics-controlled mesh with the

element size specified as "extra fine" and "extremely fine" for tissue and probe domain, respectively. The numerical solutions were obtained using the "PARADISO" method. The simulations were run on a midrange workstation with Intel(R) Xeon(R) E5-1620 CPU and 8 GB RAM.

The numerical solution was broken down into 3 steps: (i) the volumetric power output, P, was obtained from equation (2); (ii) the temperature distribution was determined as a function of time, using the volumetric power output from step (i) as heat generation term in equation (3); and (iii) the thermal dose was calculated as a function of time, using the temperature history, and was used as the input to equation (4). For all FEM analyses, time-dependent studies for 15 mins in 10 s steps.

Data Availability

The data used to support the findings of this study are included within the article.

Conflicts of Interest

The authors declare that they have no conflicts of interest.

Acknowledgments

This work was made possible with financial support from the Building a New Generation of Academics in Africa (BANGA-Africa) project which is funded by the Carnegie Corporation of New York.

References

[1] L. A. Torre, F. Bray, R. L. Siegel, J. Ferlay, J. Lortet-Tieulent, and A. Jemal, "Global cancer statistics, 2012," *CA: A Cancer Journal for Clinicians*, vol. 65, no. 2, pp. 87–108, 2015.

[2] J. Bruix and M. Sherman, "Management of hepatocellular carcinoma," *Hepatology*, vol. 42, no. 5, pp. 1208–1236, 2005.

[3] D. Haemmerich and D. J. Schutt, "Sequential activation of multiple grounding pads reduces skin heating during radiofrequency tumor ablation," *International Journal of Hyperthermia*, vol. 23, no. 7, pp. 555–566, 2009.

[4] S. D. Huffman, N. P. Huffman, R. Lewandowski, and D. Brown, "Radiofrequency ablation complicated by skin burn," *Seminars in Interventional Radiology*, vol. 28, no. 2, pp. 179–182, 2011.

[5] H. Ibrahim, B. Finta, and J. Rind, "Incidence and factors predicting skin burns at the site of indifferent electrode during radiofrequency catheter ablation of cardiac arrhythmias," *Cardiology Research and Practice*, vol. 2016, Article ID 5265682, 4 pages, 2016.

[6] K. Steinke, S. Gananadha, J. King, J. Zhao, and D. L. Morris, "Dispersive pad site burns with modern radiofrequency ablation equipment," *Surgical Laparoscopy, Endoscopy & Percutaneous Techniques*, vol. 13, no. 6, pp. 366–371, 2003.

[7] P. K. Jain, X. Huang, I. H. El-Sayed, and M. A. El-Sayed, "Noble metals on the nanoscale: optical and photothermal properties and some applications in imaging, sensing, biology, and medicine," *Accounts of Chemical Research*, vol. 41, no. 12, pp. 1578–1586, 2008.

[8] L. H. Reddy, J. L. Arias, J. Nicolas, and P. Couvreur, "Magnetic nanoparticles: Design and characterization, toxicity and biocompatibility, pharmaceutical and biomedical applications," *Chemical Reviews*, vol. 112, no. 11, pp. 5818–5878, 2012.

[9] A. C. Anselmo and S. Mitragotri, "A review of clinical translation of inorganic nanoparticles," *AAPS Journal*, vol. 17, no. 5, pp. 1041–1054, 2015.

[10] K. Kan-Dapaah, N. Rahbar, and W. Soboyejo, "Implantable magnetic nanocomposites for the localized treatment of breast cancer," *Journal of Applied Physics*, vol. 116, no. 23, article 233505, 2014.

[11] K. Kan-Dapaah, N. Rahbar, A. Tahlil, D. Crosson, N. Yao, and W. Soboyejo, "Mechanical and hyperthermic properties of magnetic nanocomposites for biomedical applications," *Journal of the Mechanical Behavior of Biomedical Materials*, vol. 49, pp. 118–128, 2015.

[12] K. Kan-Dapaah, N. Rahbar, and W. Soboyejo, "Novel magnetic heating probe for multimodal cancer treatment," *Medical Physics*, vol. 42, no. 5, pp. 2203–2211, 2015.

[13] K. Kan-Dapaah, O. A. Asimeng, S. K. Kwofie, and A. Yaya, "A plasmonic photo-thermal probe for thermoablation of post-operative breast cancer cells," *Cogent Engineering*, vol. 4, no. 1, article 1331966, 2017.

[14] J. Carrey, B. Mehdaoui, and M. Respaud, "Simple models for dynamic hysteresis loop calculations of magnetic single-domain nanoparticles: application to magnetic hyperthermia optimization," *Journal of Applied Physics*, vol. 109, no. 8, article 083921, pp. 1–17, 2011.

[15] H. H. Pennes, "Analysis of tissue and arterial blood temperatures in the resting human forearm," *Journal of Applied Physiology*, vol. 1, no. 2, pp. 93–122, 1948.

[16] S. Jacques, S. Rastegar, S. Thomsen, and M. Motamedi, "The role of dynamic changes in blood perfusion and optical properties in laser coagulation of tissue," *IEEE Journal of Selected Topics in Quantum Electronics*, vol. 2, pp. 922–933, 1996.

[17] R. Agah, J. A. Pearce, A. J. Welch, and M. Motamedi, "Rate process model for arterial tissue thermal damage: implications on vessel photocoagulation," *Lasers in Surgery and Medicine*, vol. 15, no. 2, pp. 176–184, 1994.

[18] I. A. Chang and U. D. Nguyen, "Thermal modeling of lesion growth with radiofrequency ablation devices," *BioMedical Engineering Online*, vol. 3, no. 1, pp. 1–19, 2004.

[19] F. Duck, *Physical Properties of Tissue: A Comprehensive Reference Book*, Academic Press, New York, NY, USA, 1990.

[20] S. Tungjitkusolmun, S. T. Staelin, D. Haemmerich et al., "Three-dimensional finite-element analyses for radiofrequency hepatic tumor ablation," *IEEE Transactions on Biomedical Engineering*, vol. 49, no. 1, pp. 3–9, 2002.

[21] D. Erickson, D. Sinton, and D. Li, "Joule heating and heat transfer in poly(dimethylsiloxane) microfluidic systems," *Lab on a Chip*, vol. 3, no. 3, p. 141, 2003.

[22] R. E. Rosensweig, "Heating magnetic fluid with alternating magnetic field," *Journal of Magnetism and Magnetic Materials*, vol. 252, pp. 370–374, 2002.

[23] Q. A. Pankhurst, J. Connolly, S. K. Jones, and J. Dobson, "Applications of magnetic nanoparticles in biomedicine," *Journal of Physics D: Applied Physics*, vol. 36, no. 13, pp. 167–181, 2003.

[24] R. Hergt, S. Dutz, R. Müller, and M. Zeisberger, "Magnetic particle hyperthermia: nanoparticle magnetism and materials development for cancer therapy," *Journal of Physics: Condensed Matter*, vol. 18, no. 38, pp. 2919–2934, 2006.

[25] S. N. Goldberg, P. F. Hahn, K. K. Tanabe et al., "Percutaneous radiofrequency tissue ablation: does perfusion-mediated

tissue cooling limit coagulation necrosis?," *Journal of Vascular and Interventional Radiology*, vol. 9, no. 1, pp. 101–111, 1998.

[26] W. Andrä, C. G. d'Ambly, R. Hergt, I. Hilger, and W. A. Kaiser, "Temperature distribution as function of time around a small spherical heat source of local magnetic hyperthermia," *Journal of Magnetism and Magnetic Materials*, vol. 194, no. 1–3, pp. 197–203, 1999.

[27] S. Dutz and R. Hergt, "Magnetic nanoparticle heating and heat transfer on a microscale: basic principles, realities and physical limitations of hyperthermia for tumour therapy," *International Journal of Hyperthermia*, vol. 29, no. 8, pp. 790–800, 2013.

[28] M. Omata, L. A. Lesmana, R. Tateishi et al., "Asian pacific association for the study of the liver consensus recommendations on hepatocellular carcinoma," *Hepatology International*, vol. 4, no. 2, pp. 439–474, 2010.

[29] T. Shibata, Y. Iimuro, Y. Yamamoto et al., "Small hepatocellular carcinoma: comparison of radio-frequency ablation and percutaneous microwave coagulation therapy," *Radiology*, vol. 223, no. 2, pp. 331–337, 2002.